Axisymmetric Drainage in Hydrophobic Porous Media Micromodels

A. Cuenca, M. Chabert, M. Morvan, H. Bodiguel

Dossier

This paper is a part of the hereunder thematic dossier published in OGST Journal, Vol. 67, No. 6, pp. 883-1039 and available online here

Cet article fait partie du dossier thématique ci-dessous publié dans la revue OGST, Vol. 67, n°6, pp. 883-1039 et téléchargeable ici

DOSSIER Edited by/Sous la direction de : **B. Bazin**

Challenges and New Approaches in EOR

Défis et nouvelles approches en EOR

Oil & Gas Science and Technology – Rev. IFP Energies nouvelles, Vol. 67 (2012), No. 6, pp. 883-1039

883 > Editorial

887 > *Some Key Features to Consider When Studying Acrylamide-Based Polymers for Chemical Enhanced Oil Recovery*
Quelques caractéristiques clés à considérer lors de l'étude des polymères à base d'acrylamide en vue de leur utilisation pour la récupération assistée chimique du pétrole
A. Thomas, N. Gaillard and C. Favero

903 > *Hydrophobically Modified Sulfonated Polyacrylamides for IOR: Correlations between Associative Behavior and Injectivity in the Diluted Regime*
Polyacrylamides sulfonés modifiés hydrophobes pour la RAH : corrélations entre le caractère associatif et l'injectivité en régime dilué
G. Dupuis, D. Rousseau, R. Tabary, J.-F. Argillier and B. Grassl

921 > *Normal Stresses and Interface Displacement: Influence of Viscoelasticity on Enhanced Oil Recovery Efficiency*
Contraintes normales et déplacement d'interface : influence de la viscoélasticité sur l'efficacité de la récupération assistée
J. Avendano, N. Pannacci, B. Herzhaft, P. Gateau and P. Coussot

931 > *Mechanical Degradation Onset of Polyethylene Oxide Used as a Hydrosoluble Model Polymer for Enhanced Oil Recovery*
Seuil de dégradation mécanique de solutions de polymères utilisés en récupération assistée des hydrocarbures
A. Dupas, I. Hénaut, J.-F. Argillier and T. Aubry

941 > *Injecting Large Volumes of Preformed Particle Gel for Water Conformance Control*
Injection d'importants volumes de gel de type GPP (gel à particules préformées) pour le contrôle du balayage en injection d'eau dans les réservoirs matures
Baojun Bai, Mingzhen Wei and Yuzhang Liu

953 > *Axisymmetric Drainage in Hydrophobic Porous Media Micromodels*
Drainage en géométrie axisymétrique dans des milieux poreux hydrophobes à deux dimensions
A. Cuenca, M. Chabert, M. Morvan and H. Bodiguel

963 > *Effect of Added Surfactants on the Dynamic Interfacial Tension Behaviour of Alkaline/Diluted Heavy Crude Oil System*
Effet de l'ajout de tensioactifs sur le comportement dynamique de la tension interfaciale du système solution alcaline/brut dilué
S. Trabelsi, A. Hutin, J.-F. Argillier, C. Dalmazzone, B. Bazin and D. Langevin

969 > *Prediction of Surfactants' Properties using Multiscale Molecular Modeling Tools: A Review*
Prédiction de propriétés des tensioactifs à l'aide d'outils de modélisation moléculaire : une revue
B. Creton, C. Nieto-Draghi and N. Pannacci

983 > *Modeling Chemical EOR Processes: Some Illustrations from Lab to Reservoir Scale*
Modélisation des procédés EOR chimiques : du laboratoire au réservoir
F. Douarche, D. Rousseau, B. Bazin, R. Tabary, P. Moreau and M. Morvan

999 > *Analysis of Heavy Oil Recovery by Thermal EOR in a Meander Belt: From Geological to Reservoir Modeling*
Analyse de la récupération d'huile lourde par procédé thermique dans une barre de méandre : du modèle géologique à la modélisation de réservoir
R. Deschamps, N. Guy, C. Preux and O. Lerat

1019> *Numerical Modeling of Thermal EOR: Comprehensive Coupling of an AMR-Based Model of Thermal Fluid Flow and Geomechanics*
Modélisation numérique d'EOR thermique : couplage complet entre un modèle d'écoulement thermique basé sur une discrétisation adaptative et la géomécanique
N. Guy, G. Enchéry and G. Renard

1029> *Evolution of Seismic Velocities in Heavy Oil Sand Reservoirs during Thermal Recovery Process*
Évolution des vitesses sismiques dans les réservoirs de sables bitumineux au cours des procédés de récupération thermique
J.-F. Nauroy, D.H. Doan, N. Guy, A. Baroni, P. Delage and M. Mainguy

IFP Energies nouvelles

Oil & Gas Science and Technology – Rev. IFP Energies nouvelles, Vol. 67 (2012), No. 6, pp. 953-962

DOI: 10.2516/ogst/2012050

Dossier
Challenges and New Approaches in EOR
Défis et nouvelles approches en EOR

Axisymmetric Drainage in Hydrophobic Porous Media Micromodels

A. Cuenca[1], M. Chabert[2*], M. Morvan[2] and H. Bodiguel[1]

1 Univ. Bordeaux, LOF, CNRS UMR 5258, 33600 Pessac - France
2 Rhodia, LOF, CNRS UMR 5258, 33600 Pessac - France
e-mail: amandine.cuenca-exterieur@eu.rhodia.com - max.chabert@eu.rhodia.com - mikel.morvan@eu.rhodia.com - hugues.bodiguel@u-bordeaux1.fr

* Corresponding author

Résumé — Drainage en géométrie axisymétrique dans des milieux poreux hydrophobes à deux dimensions — Nous présentons une étude de phénomènes de drainage dans des micromodèles bidimensionnels de milieu poreux s'appuyant sur des méthodes modernes de microfabrication et d'analyse. Le drainage d'huile par des solutions aqueuses est étudié à de faibles nombres capillaires (Ca) communément rencontrés lors des opérations d'extraction pétrolière. Nous utilisons deux types de micromodèles mouillables à l'huile : le premier est basé sur une méthode de déposition innovante permettant d'obtenir des monocouches de billes de verre de taille micronique, tandis que le second est microfabriqué dans du verre à partir de réseaux poreux aléatoires générés informatiquement. Chacun des modèles utilise un schéma d'injection central dans une géométrie radiale, ce qui engendre une variation continue du nombre capillaire pendant le drainage.
Nous menons tout d'abord une analyse du drainage à l'échelle globale du micromodèle en couplant analyse d'image et mesures de pression et de débit. Les paramètres de base tels que perméabilité, porosité et saturation résiduelle en huile des modèles sont extraits dans cette première phase. Nous exploitons ensuite les possibilités de visualisation offertes par les micromodèles transparents pour mener une analyse locale du phénomène d'invasion. Les saturations locales et la largeur de front sont mesurées en fonction du nombre capillaire local. De façon intéressante, du fait de la géométrie radiale, nos expériences permettent de tracer continûment les courbes de désaturation capillaire sur plusieurs décades. Comme inféré, mais jamais observé précisément, les mesures de diverses expériences se regroupent sur une courbe maîtresse pour un micromodèle donné. Nous observons cependant des différences notables entre les deux types de micromodèle. Ces observations sont discutées à la lumière des différences géométriques existant entre les deux micromodèles à l'échelle du pore.

Abstract* — *Axisymmetric Drainage in Hydrophobic Porous Media Micromodels — *We present studies of axisymmetric drainage in two-dimensional micromodels of porous media using up to date microfabrication and image analysis methods. Drainage of model oil by aqueous solutions is studied at low capillary numbers (Ca) typically encountered during oil recovery operations. We use two types of oil-wet micromodels: one is based on a deposition method for creating a random monolayer of micronic glass beads, while the other is made using computer generated random networks etched in glass using wet-lithography. Both models have a central injection scheme and a radial geometry, resulting in a continuous variation of the capillary number during the course of drainage.*
We first carry out an analysis of experiments at global micromodel scale using computer based image analysis coupled with flow rates and pressure drop measurements. Basic relevant parameters such as permeability, porosity of the micromodel and residual oil in place after waterflooding are extracted.

We then take advantage of the ease of observation in transparent micromodels to investigate the drainage phenomenon at local scale. Local saturation and front width are measured as a function of the local capillary number. Interestingly, because of the radial flow geometry, our experiments allow a continuous plotting of the micromodels capillary desaturation curve on several decades. As expected but never precisely observed, all points of various experiments collapse on a single capillary desaturation curve for a given micromodel. However, we observe dissimilar behaviors between the two types of micromodels. We discuss this phenomenon in light of the pore scale geometrical differences between the two models.

INTRODUCTION

Capillary desaturation curves are a long-lived paradigm in enhanced oil recovery applications [1]. In typical secondary oil recovery operations (oil drainage by an aqueous solution), these curves basically describe the decrease in residual oil saturation when the system capillary number – dimensionless ratio of viscous to capillary forces – increases. Numerous experiments carried out in three dimensional (3D) rock cores sustain the existence of a unique desaturation curve for a given porous media geometry and wettability [1]. In integrated studies dedicated to chemical EOR, this curve is a key component for pilot simulations based on lab measurements. However, in most practical situations, due to intrinsic experimental limitations, the capillary desaturation curve used to scale-up lab core floods are based on a few data points only. Moreover, capillary desaturation theory is based on sound arguments [2] but the separated effects of oil/water InterFacial Tension (IFT), viscosity and fluid velocity on its shape were scarcely checked experimentally. In addition, most extensive core-floods experiments have been carried out in water-wet media but few information exists on capillary desaturation in oil-wet media. The latter however represents an important part of the proven world oil reserves.

In that context, from an upstream standpoint, two-dimensional (2D) micromodels have been used for more than thirty years to gain a better understanding of pore scale mechanisms affecting oil-recovery during drainage by water [3, 4]. Various parameters such as wettability of the porous media, pore and junction shapes, relative viscosities of the invading and defending fluids were observed visually and interpreted theoretically [5]. Limiting cases of Invasion-Percolation with Trapping (IPT) at low capillary numbers, Diffusion Limited Aggregation (DLA) and anti-DLA behaviors at high capillary numbers were successfully probed using this approach [6]. IPT fractal exponents were uncovered for drainage of a wetting liquid by a non-wetting one. A scaling of front heterogeneity with the capillary number was extracted and explained by local viscous effects [7-9]. Considerable progress in microfabrication technologies combined with advanced computing methods have also opened the way to the design of quantitative and reproducible micromodels experiments [10-13].

In these approaches, two main types of micromodels were used: microfabricated ones and those based on 2D randomly dispersed beads. Here, we focus on the invasion-percolation regime in these two types of models. We use conditions representative of random oil-wet media in a radial flow scheme. We first present the design and characterization of two original micromodels. Global "petrophysics-like" measurements allow us to determine the basic average properties of our systems such as permeability and porosity. We then use local measurements to characterize capillary desaturation by a continuous variation of displacement front velocity on several orders of magnitude. Front width and fractal dimension are measured and analyzed. We compare phenomena taking place in microfabricated and bead-based geometries differing by the distribution and size of heterogeneities.

1 MICROMODELS DESIGN AND CHARACTERIZATION

The two micromodels are based on different fabrication methods. The first one, hereafter denoted as "beads model" is based on a monolayer of glass beads. The second one, hereafter denoted as "glass model", is microfabricated using wet-etching on glass wafers. Both micromodels present a radial flow scheme: fluids are injected from the center and flow toward open-ended outlets of the model [5]. This configuration provides several advantages. First, the fluids directly enter the porous media from a single source point, which prevents entry-effects artifacts. In addition, due to the $1/r$ variation of fluid velocity as a function of the radial coordinate r, a continuous range of capillary numbers can be explored in a single experiment at a given flow rate. The radial flow scheme is also the most representative of what happens in a real reservoir.

1.1 Micromodel Fabrication

1.1.1 Glass Beads Micromodel

Our method is an improvement of classical 2D beads micromodels fabrication [7, 14] allowing for a quick and flexible conception. In particular, it permits the preparation of 2D random micromodels at virtually any pore scale

down to 1 µm. The fabrication is based on the adhesion of micrometer sized glass beads on transparent glass slides spin-coated with a thin layer of PolyDiMethylSiloxane (PDMS). Glass beads tend to adhere to the PDMS but not together. Thus, a random monolayer of glass beads can easily be prepared by sprinkling beads on the PDMS and removing the excess unstacked beads.

Industrial glass beads are sifted on three successive sieves with respectively 60, 53 and 40 µm grid size. In the experiments presented here, beads with sizes between 40 and 53 µm are selected. The average bead diameter, measured by image analysis on 400 specimens, is 45 µm with a 4 µm standard deviation. A 10:1 ratio PDMS / hardener mix (Sylgard 184, *Dow Corning*) is spin-coated 90 seconds at 3 000 rpm on two 76 × 52 mm, 5 mm thick glass slides (*Ediver*, France). The resulting layer thickness, measured using a mechanical profilometer (Dektak 6M, *Veeko*), is 20 ± 1 µm, which agrees qualitatively well with prediction of the lubrication theory for spin-coating. The plates are partly cured at 65°C for ten minutes in order to obtain a reticulated but still sticky PDMS film. Glass beads are sprinkled on one of the glass plates, resulting in a random adhered beads monolayer. The two glass plates are introduced back at 65°C for 24 hours. Free PDMS chains can diffuse on the surface of the glass beads, making the latter hydrophobic. Before starting an experiment, the beads monolayer is squeezed using the second glass plate with its PDMS-coated face toward the glass beads. This creates a hydrophobic random 2D micromodel *(Fig. 1)*. The system is squeezed between two thick glass plates using a custom screw press.

Micromodel surface porosity (calculated by image analysis as the ratio of beads-occupied surface to the total micromodel surface) is $\phi_b = 50\%$. The height $h_b = 30$ µm of the micromodel is estimated by measuring an average front speed for a given flow rate (see *Sect. 2.1*). This height corresponds to glass beads being partially sticked in the soft PDMS layers, as sketched in Figure 1. The permeability is calculated according to Darcy law by circulating isopropanol at constant flow rate and measuring the total pressure drop ΔP. In axisymmetric geometry the flow rate Q relates to the pressure drop ΔP as $Q = 2\pi hk\Delta P/\eta \ln(R_i/R_e)$, where k is the permeability, h the thickness of network and R_i and R_e are the inner and outer radii, respectively [1]. We experimentally recover a linear dependency of the pressure as a function of the flow rate and find $k \approx 10^{-12}$ m^2.

1.1.2 Glass Micromodel

Glass micromodels are fabricated by standard photolithography on a mask aligner (MJB4, *Suss Microtec*), followed by wet-etching combined with fusion bonding.

(1) In the rectangular bead micromodel, R_e is the half width of the rectangle.

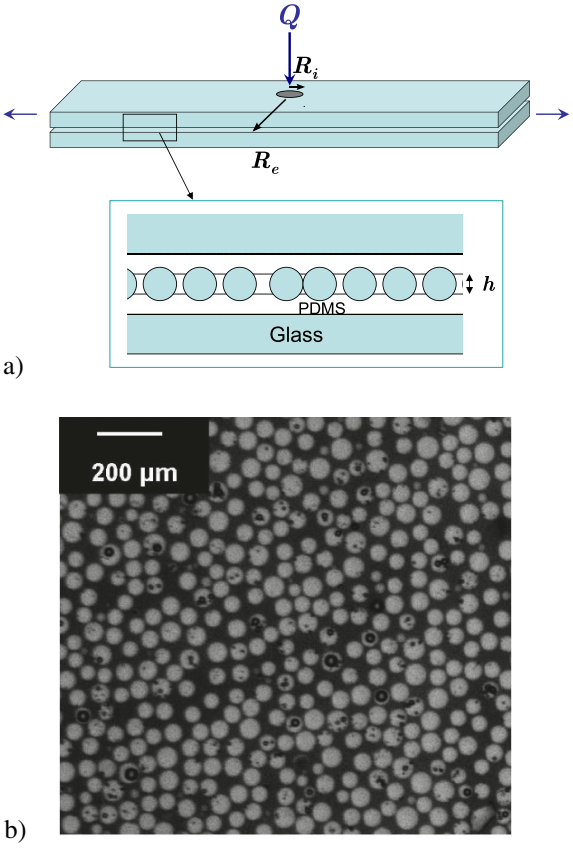

Figure 1

a) Scheme of the bead micromodel. b) Magnified image of the bead micromodel.

Random masks used for the photolithography are generated using a custom Matlab algorithm. We perform the inverse Fourrier transform of a diffraction pattern centered on k_0 that is defined by:

$$F_{ij} = \alpha_{ij} \exp\left(-(k - k_0)^2/2\sigma^2\right)/k$$

where α_{ij} are complex numbers whose real and imaginary parts are set randomly according to a uniform distribution between –1 and 1, and where $k^2 = i^2 + j^2$. This enables to choose the correlation length $2\pi/\sigma$ of the pattern resulting from the inverse Fourrier transform and its standard deviation. This pattern is thresholded to obtain a binary image, which is then skeletonized using a standard image processing algorithm. Finally, the skeleton is dilated to obtain the required channel width. This procedure is quick and easy and leads to random networks that exhibit a rather well defined correlation length. A 3 inches mask with average channel size of 10 µm is obtained by printing the network at 25 400 dpi resolution (*Selba*). The correlation length used is 0.39 mm.

A standard 7.62 cm diameter circular glass wafer (Borofloat 33, *Schott*) is protected by successive deposition

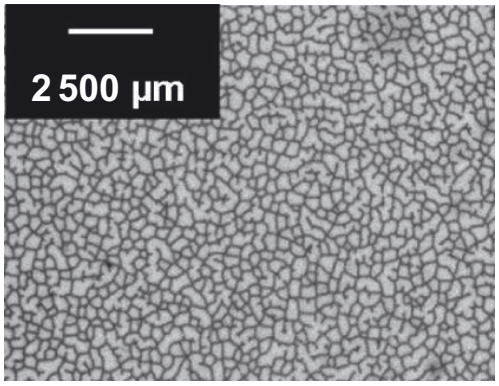

Figure 2

Magnified image of the glass micromodel filled with dyed water.

of chromium and gold in a vacuum coater (Auto 500, *BOC Edwards*). Positive resist (Microposit S1818, *Rohm and Haas*) is spin-coated on the resulting wafer and exposed through the random mask. Etching is carried out by 20 minutes immersion in a 20 wt% aqueous HF solution, corresponding to a theoretical channels depth of 15 µm. The micromodel is closed by thermal bonding with a second glass wafer in a ceramic oven (*Nabertherm*). The resulting channels are made hydrophobic using a 1 wt% octadecyltrichlorosilane (90%, *Sigma*) solution in toluene (99%, *VWR*). Prior to treatment, the surface of the micromodel is activated for 90 seconds in an oxygen plasma cleaner (*Harrick*). The silane solution is injected in the micromodel at 1000 µL/h for 30 minutes. The micromodel is then rinsed with toluene for one hour and stored at 80°C for one night. Hydrophobicity of octadecyltrichlorosilane treated glass is comparable to that of PDMS: dodecane is totally wetting on both surfaces in presence of water.

The obtained micromodel has a surface porosity $\phi_v = 36\%$ and a permeability $k_v = 2{\cdot}10^{-12}$ m^2 (measured as in *Sect. 1.1.1*). Channels width and depth (measured using a mechanical profilometer) are 115 µm and 12 µm respectively. HF glass etching being isotropic, the final width of etched channels should be around 40 µm but under-etching occurs. The measured height is correlated by measurement of the average front speed at a given flow rate (see *Sect. 2.1*) and is also consistent with the permeability and porosity. An illustration of the glass model is presented in Figure 2.

1.2 Micromodels Characterization

Average measurements carried out on the whole micromodel are used to define basic properties of the 2D porous media such as height and permeability. An analysis of water invasion in oil saturated micromodels is then carried out using methods described in the following.

1.2.1 Materials and Methods

Dodecane (99%, viscosity η_o = 1.34 mPa.s at 25°C, *VWR*) is used as defending fluid in all experiments. The invading fluid is an aqueous solution supplemented with 4 g/L Unicert blue (*Sensient*) for visualization. Surfactants used in this study are a home-synthesized C18 alpha-olefin sulfonate (C18-AOS) and the ethoxylated alcohol Rhodasurf BC630 (*Rhodia*). Unicert blue, C18-AOS and BC630 at concentrations above Critical Micellar Concentration (CMC) respectively yield an interfacial tension (IFT) of 30, 0.5 and 5 mN/m with dodecane. All aqueous solutions are prepared using demineralized water and their viscosity η_a is 1 mPa.s. Although unfavorable, the viscosity ratio between oil and water remains close to 1 and is not supposed to produce any viscous fingering in the IPT regime, we are studying here.

Prior to each measurement, the micromodel is saturated with dodecane at high flow rate (> 1 000 µL/h) to reach 100% oil-saturation. Drainage experiments are then carried out by injection of aqueous solutions at fixed flow rates. Between each experiment, the micromodel is rinsed with isopropanol and water.

All experiments are carried out at ambient temperature in an air-conditioned dark room. Homogeneous lighting is provided by a fluorescent backlight (*StockerYale*) placed underneath the porous micromodel. Fluid propagation is recorded using a Pike F505B digital camera (*Allied Vision Technologies*, 2 452 × 2 054 pixels). Depending on the desired resolution, the camera is focused using a 25 mm objective (*Fujinar*) or an *Olympus* SZX16 binocular. Fluid flow is controlled using an *Harvard* PHD4000 syringe pump equipped with a 1 mL syringe (*Exmire*).

1.2.2 Image Analysis

Image analysis is carried out using a custom Matlab routine. Briefly, as a basis for all following operations, the background is calculated on a reference image (empty micromodel) for a given experiment. This background is used to normalize all other experiment images, in order to correct illumination heterogeneities. Threshold is set manually and images are binarized. This allows for all subsequent analysis of a given sequence, *i.e.* saturation measurements and fractal dimension extraction. Analysis is done on the whole model area for circular glass models and on a 4 × 3.3 cm rectangle for beads models.

2 RESULTS

The capillary number is not uniform in radial geometry and can be defined at a distance r from the center as:

$$\mathrm{Ca} = \frac{\eta v(r)}{\gamma} = \frac{\eta}{\gamma}\frac{Q}{2\pi r h \phi} \quad (1)$$

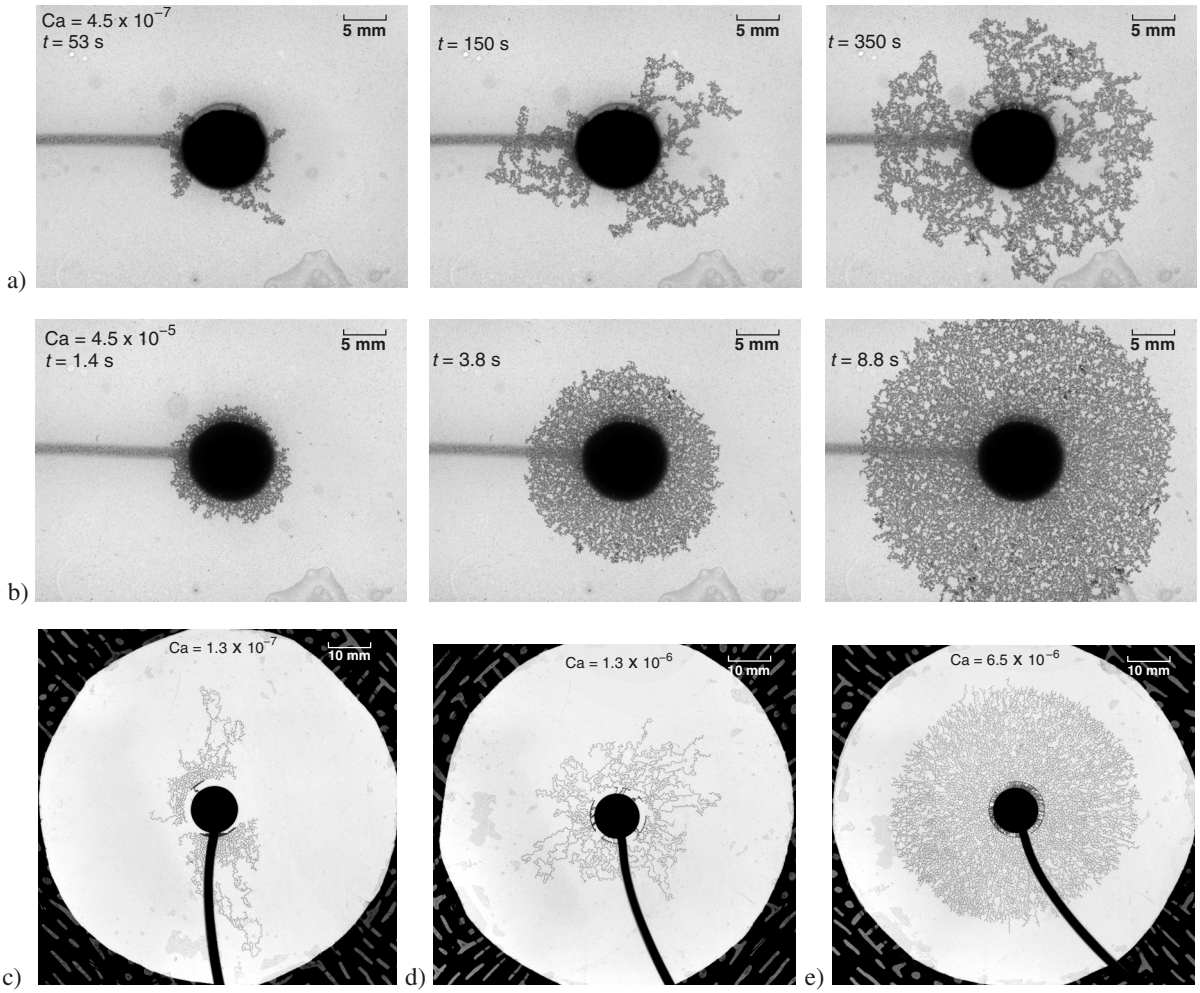

Figure 3

Examples of images taken during water invasion in the oil saturated models. a) Bead micromodel at a low flow rate of 50 μL/h (times are 53, 150 and 350 s). b) Bead micromodel at 5 000 μL/h (times are 1.4, 3.8 and 8.8 s). c) Glass micromodel at 10 μL/h (t = 130 s). d) Glass micromodel at 100 μL/h (t = 35 s). e) Glass micromodel at 500 μL/h (t = 45 s).

where $v(r)$ is the mean velocity at a distance r of the injection, η is the viscosity of the aqueous solution (invading fluid), γ the surface tension, Q the imposed flow rate, h the effective thickness of the channels and ϕ the porosity.

In the following, we first describe the observed phenomena at the global micromodel level, before taking advantage of the decrease of Ca during an experiment as discussed in Section 2.2.

2.1 Global Analysis of the Invasion

Figure 3 shows two image sequences obtained during the drainage in both micromodels. At low flow rates (for capillary numbers on the order of 10^{-7}), the invading fluids exhibit strong fingering. One or a few menisci advance at a time. Their progression is random-like and leads to the formation of a fractal pattern *(Fig. 3a)*. Typical width of the advancing front is on the order of the micromodel size for the lowest flow rates tested. At increasing flow rate, the front width decreases and the invading pattern tends to be circular, reaching the symmetry of the problem *(Fig. 3b)*. Concomitantly, the residual oil saturation and the size of the trapped clusters greatly decrease. The experiments conducted in glass micromodels *(Fig. 3c-e)* show qualitatively the same trends at a different scale. Indeed, the channels correlation lengths in the glass micromodel are about ten times higher than in the beads micromodels and can be visualized directly.

These observations of capillary fingering at low flow rate evolving towards a stable viscous front at higher flow rates are consistent with the theoretical considerations of

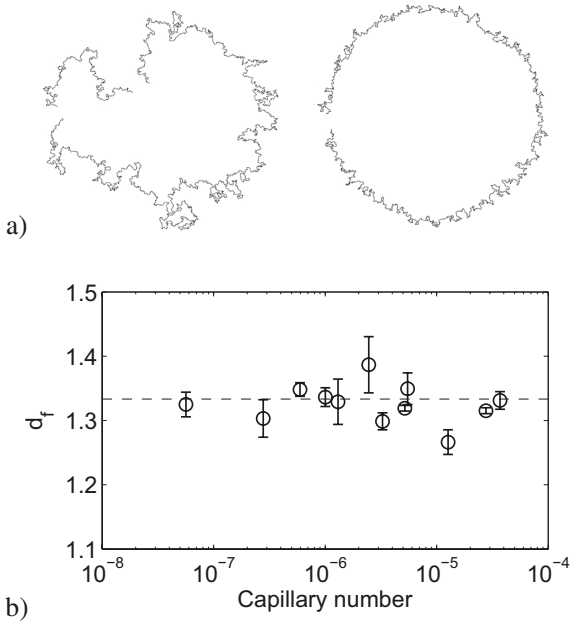

Figure 4

a) Examples of the extracted perimeter of the invasion pattern for bead micromodels (left: 50 µL/h, right: 5 000 µL/h). b) Their fractal dimensions d_f determined using a box counting algorithm are displayed on the bottom plot as a function of the capillary number of the experiment (see text for its precise definition). The fractal dimension is constant and equal to 1.33 (±0.05) in the whole range of capillary numbers tested. The dashed line indicates the theoretical value of 4/3 predicted by the invasion-percolation theory.

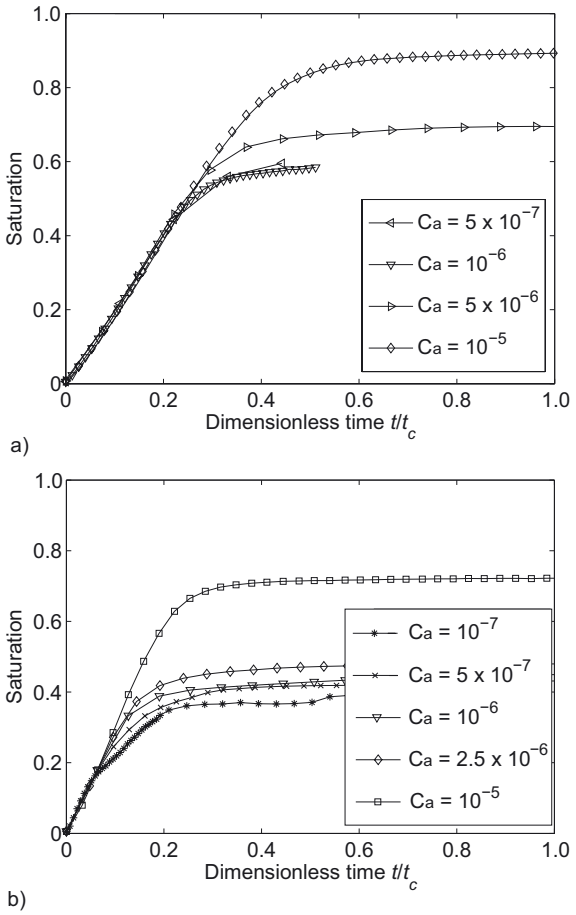

Figure 5

Global water saturation as a function of dimensionless time t/t_c (see text for the definition of t_c) for various mean capillary numbers. The mean value of Ca is defined in Equation (1), with $r = (R_e - R_i)/2$. a) Beads micromodel. b) Glass micromodel.

the invasion-percolation framework [6, 15, 16] and with previously reported micromodel experiments [7, 8]. These theories predict invasion patterns with a perimeter of fractal dimension $d_f = 4/3$ [17]. We use the box counting method to determine the fractal dimensions of the patterns' perimeter observed in the beads micromodel prior to percolation *(Fig. 4)*. The algorithm consists in counting the number of boxes N of size w required to cover the invading front. Then, the data are fitted by a power law, such that $N \propto w^{-d_f}$, for $w \in [1, 16]$ pixels. The values of d_f are plotted in Figure 4 as a function of the capillary number defined in Equation (1), with r the equivalent radius of the pattern, *i.e.* $r = \sqrt{A_w/\pi}$, where A_w is the pattern area. As shown in Figure 4, we find a fractal dimension of 1.33 that is in very good agreement with the theoretical value of 4/3. This is true in the whole range of Ca studied, which means that the basics of invasion-percolation mechanisms still hold when the front is stabilized by viscous forces. We did not perform the fractal dimension measurement in the glass micromodels experiments since the observation scale does not permit to remove the discretization of the pattern by the individual channels.

We now compute the global aqueous solution saturation S_w as a function of time for various capillary numbers in both micromodels. First, knowing the surface porosity and the imposed flow rate Q, the height h of the channels is deduced by fitting the slope of S_w with a linear relation at short times. We find $h_b = 30$ µm for the bead model and $h_g = 12$ µm for the glass model, in good agreement with microfabrication parameters. The obtained value is used to define a measurement volume $V_p = hA_t$, with A_t the total area. In order to compare various capillary regimes,

a characteristic time t_c is defined as $t_c = V_p/Q$ where Q is the applied flow rate and V_p is the measurement volume. t_c is the theoretical time for invasion of the whole observation zone by a stable radial flow in a Hele-Shaw cell configuration. Saturation S_w as a function of the dimensionless time t/t_c for various average capillary numbers in both micromodels is shown in Figure 5. It is defined by $S_w = A_w/A_t$ for the bead micromodel and by $S_w = A_w/\phi A_t$ for the glass micromodel, where A_w is the area occupied by the water phase (as determined by thresholding of the images) and A_t the total area of the image. The difference between the two definitions is due to the channel "walls'' being not resolved in thresholded images of the bead micromodel, whereas they are in the glass micromodel.

Global analysis of fluid saturations allows a direct comparison of our 2D micromodels with more complex 3D porous media. As one would expect, the global water saturation increases as a function of time. Primary drainage corresponds to micromodel invasion by the aqueous solution. After short times $t/t_c < 0.1$ used to define h, a Ca-dependent inflexion from the initial slope is observed between $t/t_c = 0.1$ and $t/t_c = 1/\phi$. This deviation starts at earlier time for low flow rates and accounts for the low final water saturations reached at low capillary number. Secondary drainage (oil displacement after percolation) appears to be negligible in most of the experiments, thus confirming the capillary-dominated regime of invasion.

Although similar trends are observed in glass and beads models, a striking difference exists between final saturations in these systems for a given capillary number. In particular, a larger spread of endpoint saturations as a function of capillary number is observed in the glass model compared to the beads model. This can be attributed to geometrical differences. Large pore size heterogeneities (of the order of one bead size) exist in the beads model, whereas pore size is homogeneous (apart from microfabrication variability) in the glass model (only channels directions are random). Our results can be related to petrophysics experiments where porous media with a wide pore size distribution generally show smoother and less dramatic variations of water saturation as a function of the capillary number than uniform ones [1].

Measurements presented here prove useful to characterize the average behavior of the micromodels. This global analysis is comparable to what can be achieved in macroscopic petrophysics experiments and shows similar trends. In addition, direct observation provides an illustration of underlying mechanisms and reflects the transition from capillary fingering towards a viscous front, accounted by the invasion-percolation theory with viscous forces. In the following section, we further exploit this visualization capability to derive a local analysis of fluids saturations and front propagation as a function of the capillary number. In particular, due to the radial flow scheme, local measurements permit a continuous analysis of saturation and front properties as a function of the capillary number.

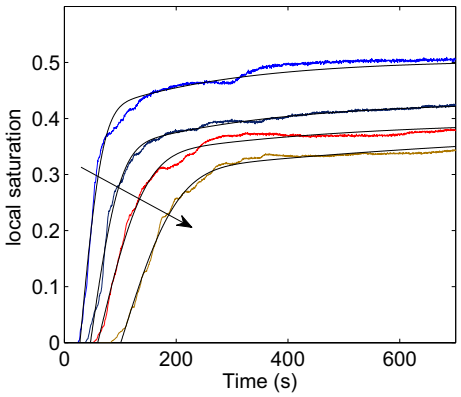

Figure 6

Examples of local saturation determined by averages on annular regions located at a distance r from the center. For the 4 curves displayed, the flow rate is 100 µL/h in the glass micromodel. The arrow indicates increasing r, that are 1.17, 1.67, 2.16 and 2.75 cm. The best fits to the data defined in Equation (2) are shown together with the experimental data.

2.2 Local Analysis of the Invasion

2.2.1 Capillary Desaturation Curves

Each observation zone is cut into 50 rings of constant width. Water saturation is measured in each ring as a function of time. One experiment at a given flow rate sweeps capillary numbers on about one order of magnitude. The capillary number is defined here locally, r appearing in Equation (1) being now the radial position of the ring of interest. To get rid of end effects, only the 40 first rings starting from the injection are taken into account for measurements.

An example of this local saturation measurement is presented in Figure 6 for several radial positions. It equals zero for short times until the front reaches the given annular region and then increases quite sharply. It further reaches steady state values in a first approximation. However, depending on the experiments, a very slow increase is also observed *(Fig. 6)*. This secondary drainage represents very low oil quantities and occurs on much longer time scale than during primary drainage. In the following, we restrict ourselves to the description of the invasion, leaving aside this second order phenomenon.

The saturation curves $s(r,t)$ are systematically fitted using an empiric function encompassing all the data. It is given by:

$$s(r,t) = s_0(r)\,\mathrm{erf}\left[\frac{t-t_0(r)}{\delta(r)}\right] + \Delta s\left[1-\exp\left(\frac{t-t_0(r)}{\tau(r)}\right)\right] \quad (2)$$

for $t > t_0(r)$ and $s(r,t) = 0$ if $t < t_0(r)$. s_0, t_0, δ, Δs and τ are fitting parameters for each annular region r.

The second term was added in order to describe the slow evolution of the saturation at long times (secondary drainage), observed in some experiments. Therefore, in the fitting procedure, the parameter τ is forced to be greater than δ by a factor of 50. Δs is furthermore a small fraction of s_0 (on the order of 5 to 20%). It should thus be considered only as a fitting trick to remove any contribution of the experiment duration. The main contribution to the saturation is well captured by the first term of Equation (2) and we focus on it solely in the following. Figure 6 displays examples of the best fits obtained, together with the experimental data. The agreement is excellent, which is expected due to the high number of fitting parameters. Our aim is here to extract from the data the essential parameters that allow to describe the drainage as a function of the flow rate and the radial position.

The physical meaning of the first term appearing in Equation (2) is rather straightforward. s_0 represents the water saturation in a location once the front has passed this location. t_0 is the time at which the most advanced finger arrives at this location, and δ is the characteristic duration of the front passing this location. When the capillary fingering is pronounced at low Ca, this last parameter should be rather high and on the contrary short when the front is sharp at high Ca.

In Figure 7, the endpoint saturations s_0 are plotted as a function of the capillary numbers for various experiments carried out at a given flow rate. Note that the capillary number is varied by three different means: the flow rate, the radial position of the annular region and the surface tension, in the case of glass beads experiments. The increase in water saturation with increasing capillary number appears on both curves. Only a trend can be extracted from beads model measurements, whereas data points from different experiments show a very good collapse in the glass model. Nevertheless, a continuous increase of aqueous solution saturation with increasing capillary number (varied by an increase in fluid velocity) is clearly demonstrated on several orders of magnitude. The important dispersion of data points in the bead micromodel can again be explained by geometrical arguments. Due to important heterogeneities, strongly capillary preferred flow paths exist in this model. It can be inferred that water patterns during drainage reproduce heterogeneities of the micromodel. Indeed, when comparing two different experiments carried out at low capillary number, the desaturation pattern has the same shape. The statistical sample size of one ring, on which measurement is carried out, is not sufficient to smooth ring-to-ring geometrical heterogeneity. On the other hand, in the regular glass micromodel, heterogeneities are minimized from ring to ring and are correctly averaged.

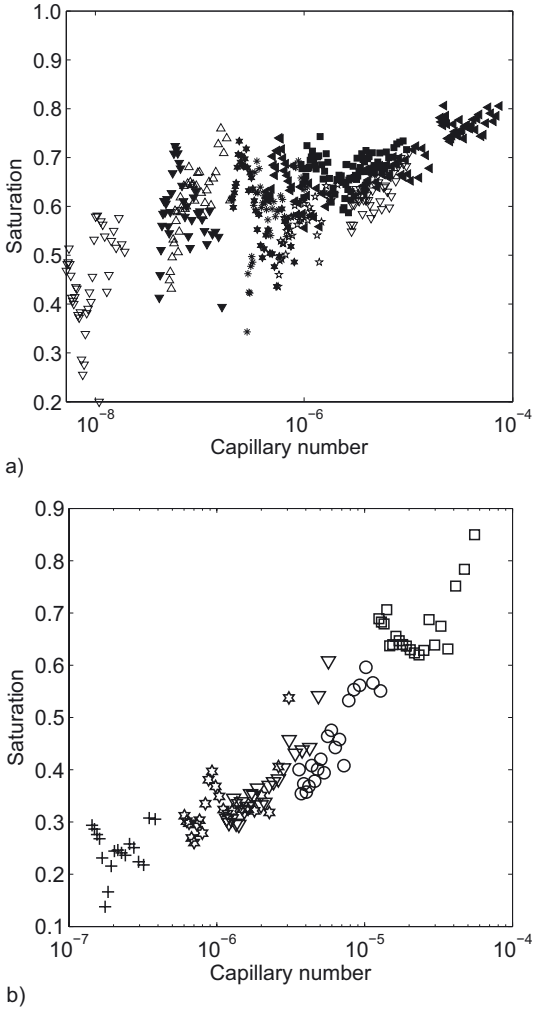

Figure 7

Water saturation s_0 after the invasion as a function of the capillary number for both micromodels. A given symbol corresponds to a given drainage experiment. a) Beads micromodel. b) Glass micromodel. The full symbols on the top figure denotes the experiments carried using the surfactant solutions.

Overall the data reported in Figure 7 for the glass micromodel demonstrate quantitatively that the saturation just after the invasion is a unique function of Ca, whatever the way Ca varies. In particular, there is no direct influence of the central injection scheme since the effect of the radial distance to the saturation is completely accounted by using a local capillary number. It can thus be concluded that capillary desaturation curves are robust quantities, relevant even at the local scale.

2.2.2 Width of the Front

Estimating the width of the front directly from the image may lead to uncertainties and definition difficulties. We thus use the local time evolution of the saturation to determine

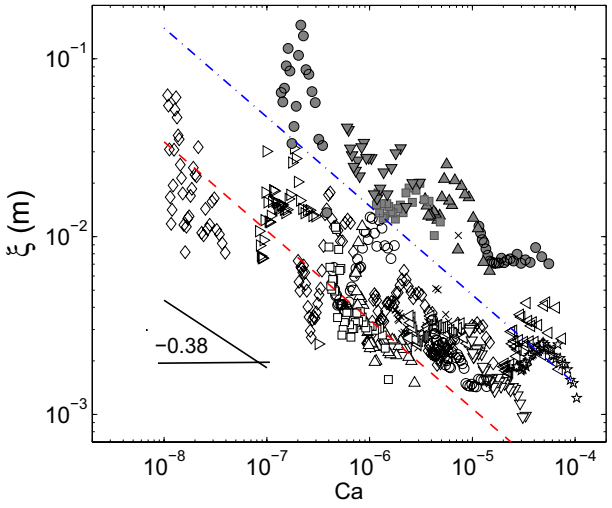

Figure 8

Width of the front deduced from the fitting parameters t_0 and δ, $\xi = \delta(r)/\partial_r t_0(r)$. Open symbol: bead micromodel. Full symbols: glass micromodel. The dashed line and the dash-dotted line respectively represent the result of the model detailed in the text (*Eq.* (5)), for the bead and the glass micromodel.

a characteristic width. Using the results of the fitting procedure, we can indeed determine the front velocity v_f, or, more precisely, the velocity of the most advanced finger by differentiating the parameter t_0 with respect to the radial distance r (see *Eq. 2*): $v_f = (\partial_r t_0)^{-1}$. The spatial width of the front is then defined by $\xi = v_f \delta$, since δ is the characteristic duration of the front passing in a given annular region. Figure 8 reports the such-determined value of ξ as a function of the capillary number, for both glass and bead micromodels. As in the previous section, the capillary number is locally defined. Similarly to the desaturation curves, the front width appears to be a unique function of the capillary number.

In agreement with the qualitative observations *(Fig. 3)*, the front width decreases when the capillary number increases. Though the data points are dispersed, the trend of the data can be described by a power-law, which leads to $\nu = 0.35$ and 0.45 (± 0.1) for the bead and glass micromodels, respectively. These values are in very good agreement with the 2D invasion-percolation theory with viscous forces, which predicts an exponent of 0.38 [15, 16]. They are also rather consistent with the value reported by Frette *et al.* [7], who use a parallel flow geometry and measure directly the front width on the images. Note however that the exponent is much closer to the theoretical one that in the experiments reported by Frette *et al*.

It is interesting to note that the width of the front is always higher, at a given capillary number, in the glass micromodel. Among the differences between the two media, the correlation length is much higher for the glass micromodel since it is about 400 μm, whereas it is set by the bead diameter of 40 μm in the bead micromodel.

These observations are explained by a rough mean field model proposed by our group in a previous communication [8]. We consider that the front width ξ is defined as the distance at which the viscous pressure increment in a developping finger overcomes the capillary pressure difference. This reads:

$$\frac{\alpha \xi \eta V}{h^2} \simeq \epsilon \gamma C, \tag{3}$$

where V is the mean velocity inside the finger, ϵ is the relative standard deviation of the capillary pressure, C the mean meniscus curvature, and α a numerical prefactor accounting for the geometry of the channel. α equals to 12 in the glass micromodel (infinite plates approximation) and should be on the order of 20 in the bead micromodel given the mean aspect ratio. The velocity V in the finger is related to the flow rate, or to the capillary number thanks to volume conservation, assuming that the mean distance separating two advancing fingers is on the order of ξ. This closure relation reads:

$$\xi \simeq \lambda \frac{\eta V/\gamma}{\mathrm{Ca}} \tag{4}$$

where λ is the correlation length, *i.e.* the characteristic distance between two pores. It equals 0.39 mm for the glass micromodel and is on the order of the bead diameter in the bead micromodel. Combining the two previous equations, we obtain the following prediction for the front width:

$$\xi \simeq 0.27 \lambda \sqrt{\frac{\Gamma \epsilon}{\mathrm{Ca}}} \tag{5}$$

where we have introduced a geometrical constant $\Gamma = Ch^2/\alpha\lambda$, and where the prefactor 0.27 was estimated numerically in Reference [8]. Estimation of Γ for the glass and bead micromodels leads to 0.1 and 2×10^{-2}, respectively. ϵ is not known *a priori* but should be on the order of unity (2). Assuming $\epsilon \approx 1$, we obtain a reasonable agreement with the experimental data as shown by the two straight lines based in Equation (5) with the above detailed parameters and displayed in Figure 8.

Although a numerical agreement is a nice output of this model, these results should be taken with care since we do not have a quantitative access to all the parameters. Let us also mention that it does not fully agree with the invasion-percolation prediction according to $\xi \sim \mathrm{Ca}^{-0.38}$. Nevertheless, this model captures the essential difference observed between the two micromodels: the correlation length of the

(2) In the bead micromodel, the pore size distribution is indeed of the order of the bead size. For the glass micromodel, it is rather difficult to estimate the pore size distribution since it originates from imperfections in the microfabrication process.

porous media has a strong impact on the invasion front, with increasing correlation lengths leading to much more disperse fronts.

CONCLUSION

This study on oil drainage in two-dimensional hydrophobic porous media enables to draw two important conclusions relevant to oil recovery operations. On the one hand, capillary desaturation curves appear to be robust quantities, not only at the global Darcy scale but also on the local scale. On the other hand, local pore scale geometry of a given porous media has a tremendous influence both on desaturation curves and on capillary driven fingering fronts. This can have strong practical implications in industrial applications such as oil recovery in locally heterogeneous porous media. A focus of future work should be extrapolation of these model results to real porous media with more complex geometrical correlations of pore size and distributions. Indeed, using these models to extrapolate continous capillary desaturation curves from real porous media would represent a breakthrough by permitting quicker and more precise access to data needed for reservoir-scale simulations.

REFERENCES

1 Lake L.W. (1989) *Enhanced oil recovery*, Prentice Hall, Englewood Cliffs, N.J., ISBN 0132816016.

2 Larson R.G., Davis H.T., Scriven L.E. (1981) Displacement of residual nonwetting fluid from porous media, *Chem. Eng. Sci.* **36**, 1, 75-85.

3 Ng K.M., Davis H.T., Scriven L.E. (1978) Visualization of blob mechanics in flow through porous media, *Chem. Eng. Sci.* **33**, 8, 1009-1017.

4 Lenormand R., Zarcone C., Sarr A. (1983) Mechanisms of the displacement of one fluid by another in a network of capillary ducts, *J. Fluid Mech.* **135**, 337–353.

5 Lenormand R. (1990) Liquids in porous media, *J. Phys. Condens. Matter* **2**, SA79.

6 Lenormand R. (1989) Flow through porous-media – limits of fractal patterns, *Proc. R. Soc. Lond. A* **423**, 1864, 159-168.

7 Frette O.I., Maloy K.J., Schmittbuhl J., Hansen A. (1997) Immiscible displacement of viscosity-matched fluids in two-dimensional porous media, *Phys. Rev. E* **55**, 3, 2969-2975.

8 Cottin C., Bodiguel H., Colin A. (2010) Drainage in two-dimensional porous media: From capillary fingering to viscous flow, *Phys. Rev. E* **82**, 4, 046315-046324.

9 Cottin C., Bodiguel H., Colin A. (2011) Influence of wetting conditions on drainage in porous media: A microfluidic study, *Phys. Rev. E* **84**, 2, 026311-026317.

10 Perrin C.L., Tardy P.M.J., Sorbie K.S., Crawshaw J.C. (2006) Experimental and modeling study of newtonian and non-newtonian fluid flow in pore network micromodels, *J. Colloid Interface Sci.* **295**, 2, 542-550.

11 Theodoropoulou M.A., Sygouni V., Karoutsos V., Tsakiroglou C.D. (2005) Relative permeability and capillary pressure functions of porous media as related to the displacement growth pattern, *Int. J. Multiphase Flow* **31**, 10-11, 1155-1180.

12 Romano M., Chabert M., Cuenca A., Bodiguel H. (2011) Strong influence of geometrical heterogeneity on drainage in porous media, *Phys. Rev. E* **84**, 065302-065305.

13 Tsakiroglou C.D., Avraam D.G., Payatakes A.C. (2007) Transient and steady-state relative permeabilities from two-phase flow experiments in planar pore networks, *Adv. Water Resour.* **30**, 9, 1981-1992.

14 Lovoll G., Meheust Y., Toussaint R., Schmittbuhl J., Maloy K.J. (2004) Growth activity during fingering in a porous hele-shaw cell, *Phys. Rev. E* **70**, 2, 026301-026313.

15 Wilkinson D. (1986) Percolation effects in immiscible displacement, *Phys. Rev. A* **34**, 2, 1380-1391.

16 Xu B., Yortsos Y.C., Salin D. (1998) Invasion percolation with viscous forces, *Phys. Rev. E* **57**, 1, 739-751.

17 Grossman T., Aharony A. (1986) Structure and perimeters of percolation clusters, *J. Phys. A: Math. Gen.* **19**, 12, L745-L751.

Final manuscript received in June 2012
Published online in January 2013